Online-Journals.org

iJOE International Journal of Online and Biomedical Engineering

iJOE | eISSN: 2626-8493 | Vol. 22 No. 3 (2026) | OPEN ACCESS

https://doi.org/10.3991/ijoe.v22i03.59657

PAPER

A Wearable Strain Sensor Based on 3D Silicone Printing with Composite Structure Design

Jiun-Hung Lin (✉)

National Kaohsiung University of Science and Technology, Kaohsiung, Taiwan

jhlin001@nkust.edu.tw

ABSTRACT

Flexible strain sensors hold significant potential in wearable electronics and human motion tracking; however, achieving a balance among sufficient measurement range, low hysteresis response, and reliable skin adhesion remains challenging. In this study, a wearable strain sensor was developed using 3D-printed silicone, and the performance of a single-layer conductive silicone design (P1) was compared with a multilayer configuration integrating an adhesive interface and medical-grade artificial skin (P2). Results show that P2 successfully extends the measurable displacement range to 10 mm and reduces hysteresis from 0.26 to 0.03 at 3 mm strain, while maintaining stable cyclic performance (standard deviation ± 0.018). The multilayer architecture improves repeatability under repeated stretching by stabilizing the conductive network and enhancing skin-attachment reliability. Human testing further demonstrates that P2 can reliably track wrist motion within 0°–30°, with resistance changes closely aligned to IMU-derived angle signals and without noticeable baseline drift. Overall, this work presents a cost-effective, skin-compatible silicone strain sensor suitable for wearable human motion monitoring, highlighting its potential for applications in health tracking and rehabilitation-related movement analysis.

KEYWORDS

flexible strain sensor, hysteresis effect, 3D silicone printing, wearable monitoring, multilayer structure

1 INTRODUCTION

Flexible and wearable electronic technologies have emerged as key drivers in the advancement of smart healthcare, rehabilitation engineering, and human–machine interaction systems [1]–[3]. Among them, flexible strain sensors play a crucial role in personal health monitoring and motion capture, as they enable real-time and continuous measurement of biomechanical signals such as skin deformation, joint movement, and muscle activity [4]–[5]. Recent advances in smart wearable

Lin, J.-H. (2026). A Wearable Strain Sensor Based on 3D Silicone Printing with Composite Structure Design. *International Journal of Online and Biomedical Engineering (iJOE)*, 22(3), pp. 58–72. https://doi.org/10.3991/ijoe.v22i03.59657

Article submitted 2025-11-15. Revision uploaded 2025-12-17. Final acceptance 2025-12-18.

technologies have further demonstrated the potential of sensor-based systems for abnormal gait detection and remote health monitoring through Internet of Things (IoT) integration [6], [7]. To function reliably on dynamic and compliant human skin surfaces, these sensors must exhibit high mechanical compliance, stretchability, and long-term adhesion capability, particularly when applied to high-mobility body regions such as the wrist or knee joints [8]. However, achieving a balance between sufficient sensing range, low hysteresis response, and stable attachment performance in practical wearable applications remains a significant engineering challenge [9]–[11].

In previous work, the improvement of flexible strain sensor performance has primarily relied on material-oriented strategies, such as incorporating carbon-based fillers, liquid metals, or conductive polymers to enhance electrical conductivity and strain responsiveness [12]–[15]. Zhao et al. [16] reported that stretchable materials and microstructural engineering represent the two major research directions toward achieving high-performance sensing systems. Following these approaches, various material architectures demonstrating high sensitivity and durability have been developed, including the graphene–silicone composite proposed by Shi et al. [17] with a gauge factor (GF) of 27.7–164.5, and the gradient carbon nanotube structure introduced by Liang et al. [18], which achieved a GF of 13.5 and a strain limit exceeding 550%. Despite their promising potential, these material-based strategies are often constrained by viscoelastic behavior, conductive network relaxation, and long-term degradation [19]–[23], which may lead to loss of conductive pathways or signal drift during repeated stretching cycles [24]–[27]. Recent studies have further confirmed that achieving low hysteresis while maintaining stable skin adhesion remains a significant challenge for practical wearable applications [28], [29].

To overcome these limitations, recent research has increasingly shifted toward structure-oriented design strategies, leveraging geometric engineering, multilayer architectures, or interfacial modification to improve measurement stability [30]–[37]. Recent studies—such as the origami-inspired configuration by Huang et al. [10] and the graded-stiffness sliding mechanism proposed by Xue et al. [11]—have demonstrated that structural engineering can effectively reduce hysteresis and enhance strain sensing capability. However, these approaches often require complex fabrication procedures, high-cost materials, or microfabrication techniques, making them impractical for scalable wearable applications or mass production scenarios [38]. Moreover, many existing sensors still encounter challenges such as signal saturation, nonlinear response, and insufficient repeatability when deployed in large-displacement monitoring tasks, including athletic motion tracking or joint movement assessment [27].

Therefore, this study proposes a flexible strain sensor design strategy centered on process simplification and structural integration to address hysteresis effects and improve large-displacement sensing performance in wearable applications. A single-layer conductive silicone sensor (P1) was fabricated using a 3D silicone printing process, followed by the development of a multilayer adhesive-integrated configuration (P2) incorporating a bonding layer and artificial skin substrate. This structural enhancement provides improved conformal adhesion, strain distribution capability, and signal recovery behavior. Through systematic performance evaluation and human motion tracking experiments, the P2 design demonstrated superior sensing range, cyclic stability, and wearable monitoring performance compared with P1. The proposed approach offers a cost-effective, scalable, and user-friendly sensing solution, providing practical potential for integrating flexible strain sensors into motion tracking and health monitoring applications.

2 METHODS

2.1 Resistance measurement and normalization

A resistive-type flexible strain sensor measures strain by detecting changes in electrical resistance of the conductive material during deformation. According to Ohm's law, the resistance can be expressed as

$$R = \rho \frac{L}{A} \tag{1}$$

where R is the electrical resistance, ρ is the resistivity of the material, L is the length of the conductive path, and A is the cross-sectional area. When the soft conductive material is subjected to tensile deformation, the path length L increases and the cross-sectional area A decreases, both contributing to an increase in resistance R. Meanwhile, microcracks may form within the conductive path, or the contact state of the conductive filler network may change, thereby altering the effective resistivity ρ and causing further variation in resistance [13], [27].

In this study, a programmable linear translation stage was employed to provide precise displacement d. When the sensor was stretched between two ends, the resistance variation was normalized and expressed as the relative resistance change $\Delta R/R_0$, which serves as a standard index for evaluating the performance of flexible strain sensors [13], [27].

$$\frac{\Delta R}{R_0} = \frac{R - R_0}{R_0} \tag{2}$$

Here, R_0 represents the baseline resistance at the beginning of each cycle, and R denotes the measured resistance at a given time. The experimental procedure consists of a stretching phase (stretch) and a releasing phase (release), performed in a periodic and repetitive manner. This normalization process eliminates the influence of initial resistance differences among samples, ensuring consistency and comparability of measurement results under different testing conditions.

2.2 Hysteresis effect analysis

To quantitatively evaluate the difference between the stretching and releasing processes of the flexible strain sensor, the resistance–displacement curve was analyzed in detail [27]. The hysteresis effect serves as a crucial indicator for assessing the stability and repeatability of the sensor. In the experiment, the sensor was mounted on a displacement-controlled platform and subjected to stretching-releasing cycles within a displacement range of 0–d mm. The entire displacement interval was evenly divided into N sampling points. At each sampling position d_i, the relative resistance changes $\Delta R/R_0$ during the stretching and releasing phases, denoted as $y_{stretch}(d_i)$ and $y_{release}(d_i)$, were recorded.

The hysteresis area A for each cycle, it was approximated as the area enclosed between the stretching and releasing curves (corresponding to the shaded region in Figure 1) and calculated using the following equation:

$$A \approx \sum_{i=0}^{N-1} \left| y_{stretch}(d_i) - y_{release}(d_i) \right| \Delta d \tag{3}$$

where Δd represents the displacement interval $d/(N-1)$ and the unit of A is $\Delta R/R_0 \cdot mm$.

A larger value of A indicates a greater average difference between the stretching and releasing curves within a single cycle, implying a more pronounced hysteresis effect. When the same displacement is repeated over k cycles, and the hysteresis area A_j of each cycle is calculated individually, the mean hysteresis area $\bar{A}$ can be determined as

$$\bar{A} = \frac{1}{k}\sum_{j=1}^{k} A_j \tag{4}$$

The mean hysteresis area $\bar{A}$ serves as a comprehensive hysteresis index for evaluating the overall stability and repeatability of the flexible strain sensor under multiple stretching–releasing cycles.

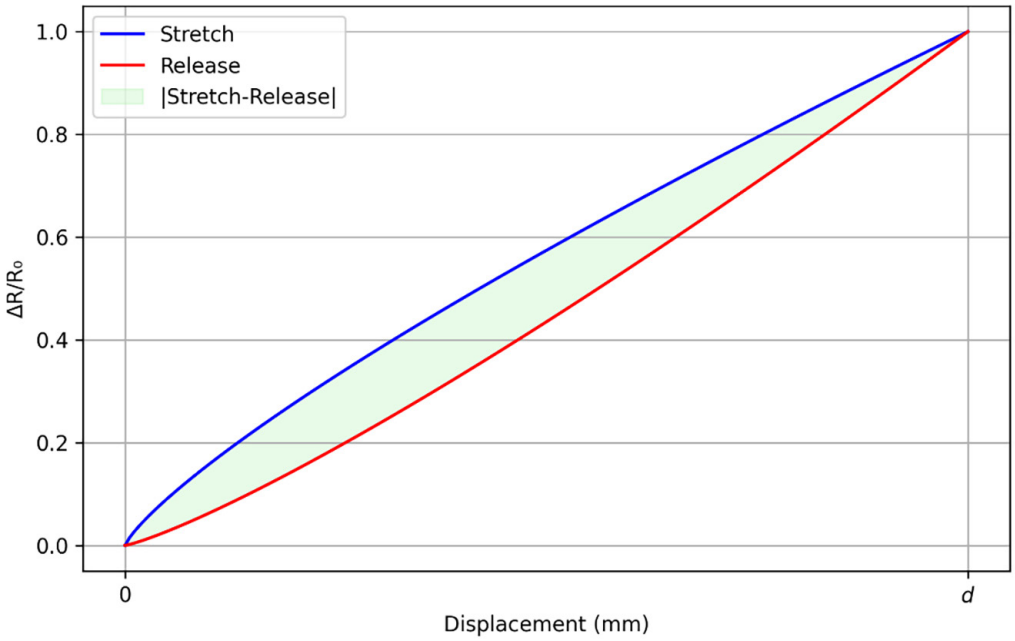

Fig. 1. Illustration of the stretching and releasing curves of relative resistance variation ($\Delta R/R_0$) versus displacement (mm) for the resistive-type flexible strain sensor

The blue curve represents the stretching process, the red curve represents the releasing process, and the light, green-shaded area indicates the hysteresis region between the two curves.

3 EXPERIMENTAL DESIGN

3.1 Fabrication process of stretchable conductive silicone using 3D printing

In this study, a 3D silicone printing system from San Draw Inc. was employed to fabricate the flexible substrate. The material used was a dual-liquid heat-curable silicone (Shore A 50) certified under ISO 10993, with the following primary mechanical properties (as specified by the manufacturer): tensile strength of approximately 1682 psi, tear strength of about 36 N, elongation at break up to 660%, and

an applicable temperature range from –50°C to 250°C. The conductive path was designed in an S-shaped geometry using a computer-aided design (CAD) to enhance strain distribution and improve extensibility (see Figure 2a).

The fabrication process was as follows: First, the printed silicone samples were cured in an oven at 60°C for two cycles of one hour each to complete thermal solidification (see Figure 2b). Next, a uniform coating of water-based stretchable silver ink (G98 series, Ink-tech Co., Ltd.) was applied onto the concave surface of the S-shaped structure (see Figure 2c). This silver ink is a low-temperature curable type, with an average silver particle size of approximately 1μm, and can be cured at room temperature or 70–100°C within 5–10 minutes, forming a film with more than 50% stretchability. Finally, the same silicone material was used for encapsulation and electrode extension at both ends (see Figure 2d), resulting in a flexible element with high extensibility and electrical conductivity.

The fabricated stretchable conductive silicone is denoted as P1, which serves as the core material for subsequent experiments in this study.

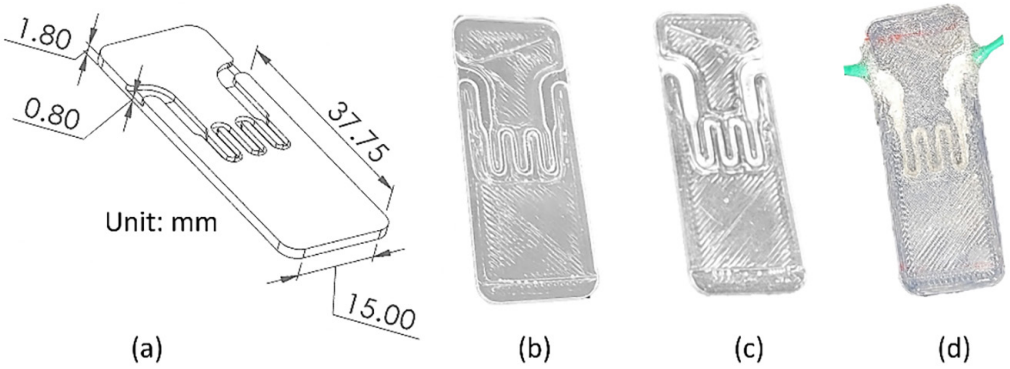

Fig. 2. Schematic illustration of the overall fabrication process of sensor P1: (a) Computer-aided design of the conductive pathway; (b) 3D silicone printing and thermal curing at 60°C for shape stabilization; (c) Coating of the structure surface with water-based stretchable silver ink to form the conductive layer; (d) Encapsulation with silicone and wire extension to complete the flexible conductive sensing element

3.2 Fabrication of a composite stretchable conductive silicone sensing element

Since the P1 sensor (single-layer conductive silicone structure) is not suitable for direct attachment to the skin, its conductive material may cause local irritation or discomfort and reduce breathability and comfort [28]. Furthermore, to achieve long-term stable adhesion, the sensor surface must possess adequate adhesive properties. To address these issues, this study adopted a hydrophilic dressing (sterile artificial skin) provided by Oriental Resources Development Limited as the bonding substrate. According to the manufacturer, this material is soft, elastic, and breathable; its hydrophilic nature enables tight adhesion to the skin, maintaining long-term attachment stability and comfort.

However, conventional artificial skin is typically adhesive only on one side and exhibits insufficient bonding strength when combined with conductive silicone. To overcome this limitation, a silicone-based double-sided medical adhesive produced by Taicend Technology Co., Ltd. was introduced as the bonding layer. According to the manufacturer, this adhesive is primarily composed of siloxane compounds, formed by the condensation of silanol and polydimethylsiloxane,

providing excellent bonding strength and structural stability during stretching, thereby preventing slippage or delamination.

Finally, the three-layer configuration composed of the conductive silicone layer, adhesive layer, and artificial skin was defined as the composite stretchable conductive silicone (P2). As shown in Figure 3, the conductive silicone was bonded to the artificial skin through the adhesive layer, forming a sensing element capable of long-term skin attachment. The exploded view illustrates how the three functional layers are stacked: the bottom artificial skin layer provides biocompatible contact with human skin, the middle adhesive layer ensures secure bonding between layers during repeated stretching, and the top conductive silicone layer (P1) serves as the strain-sensing element with measurement points at both ends for electrical signal acquisition. When an external tensile force was applied, the conductive silicone exhibited variations in electrical resistance, while the artificial skin provided soft cushioning and conformal support. This configuration is expected to enhance the mechanical stability and elastic recovery of the sensor.

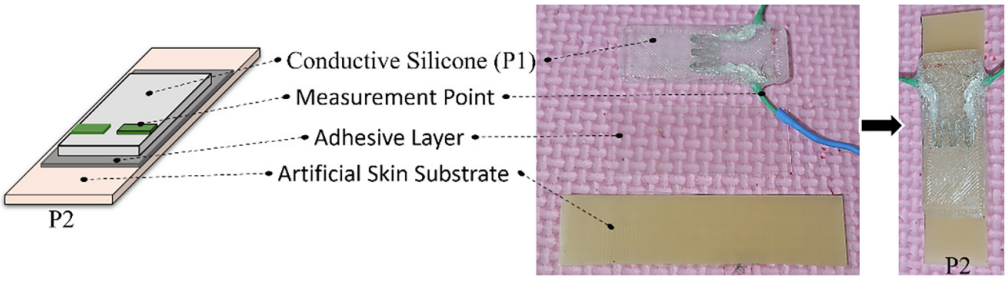

Fig. 3. Structural schematic and assembly of the composite stretchable conductive silicone sensor (P2) [(Left) Exploded view illustrating the three-layer configuration: the artificial skin substrate (bottom), the silicone-based double-sided adhesive layer (middle), and the conductive silicone P1 with measurement points (top). (Center) Photographs of the components before assembly, including the P1 element with electrode wires and the artificial skin substrate. (Right) The fully assembled P2 sensor]

3.3 Measurement platform

To evaluate the resistance–displacement characteristics of the P1 and P2 sensors, an integrated measurement platform was designed, as shown in Figure 4. The platform consists of four modules: motion control, mechanical measurement, electrical measurement, and data integration. The motion control module utilizes a data acquisition card (NI USB-6009, National Instruments Corporation) to output control signals to a stepper motor driver (TB6600, Shanghai Zhiwei Robotics Co., Ltd.), which in turn drives a stepper motor to move a linear translation stage for precise displacement control. The mechanical measurement module employs a force gauge (ZP-20N, Shenzhen Ailigu Instrument Co., Ltd.) with clamps to secure both ends of the specimen, enabling real-time measurement of the tensile force applied during stretching. The electrical measurement module uses a digital multimeter (GDM-8341, Good Will Instrument Co., Ltd.) connected to both electrode ends of the specimen to continuously record the variation in resistance with displacement.

All displacement, force, and resistance data were synchronously transmitted to a computer and integrated in real time via LabVIEW (National Instruments Corporation) software. The experimental parameters were set as follows: the stretching and releasing displacement range was adjusted according to the

experimental requirements, with 10 loading-unloading cycles and a displacement speed of approximately 0.1 mm/s. This configuration allowed simultaneous observation of the sensor's resistance variation under different displacement conditions, as well as its stability and hysteresis behavior during cyclic stretching. All experiments were conducted under room temperature conditions 25 ± 0.5°C with relative humidity maintained at 50–60%, ensuring consistency across all measurement conditions.

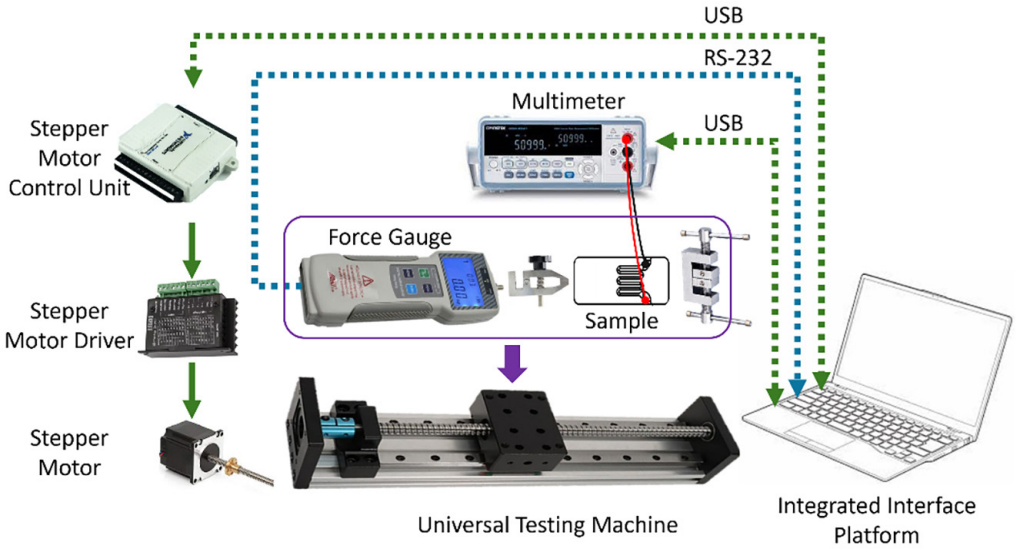

Fig. 4. Schematic diagram of the stretching measurement platform for the resistive flexible strain sensor

4 RESULTS

4.1 Comparative performance of P1 and P2 sensors

This section compares the electromechanical response characteristics of the first stage conductive silicone sensor (P1) and the second stage composite conductive silicone sensor (P2) under different displacement conditions. Figure 5 presents the relationship between the relative resistance change ($\Delta R/R_0$) and displacement for the P1 sensor at displacement amplitudes of 1 mm, 2 mm, and 3 mm. The solid line represents the stretching phase, while the dashed line corresponds to the releasing phase; the shaded area indicates the hysteresis region, and the error bars denote the standard deviation. The results show that the value of $\Delta R/R_0$ increases progressively with displacement, and the peak magnitude grows with larger displacement amplitudes. At a displacement of 3 mm, the peak value reaches approximately 0.70–0.75; at 2 mm, it is about 0.50, and at 1 mm, approximately 0.30. These results confirm that increasing tensile displacement produces a positive correlation with resistance change, consistent with the strain-induced elongation of conductive pathways within the stretchable sensing material, leading to a measurable increase in resistance.

In addition, all three curves exhibited a pronounced hysteresis effect during the release phase (dashed line) compared with the stretching phase (solid line). Specifically, under identical displacement conditions, the $\Delta R/R_0$ values in the releasing phase were consistently lower than those in the stretching phase, and this discrepancy became more evident with larger displacement amplitudes. Among the three displacement conditions, the maximum standard deviation was approximately ± 0.06.

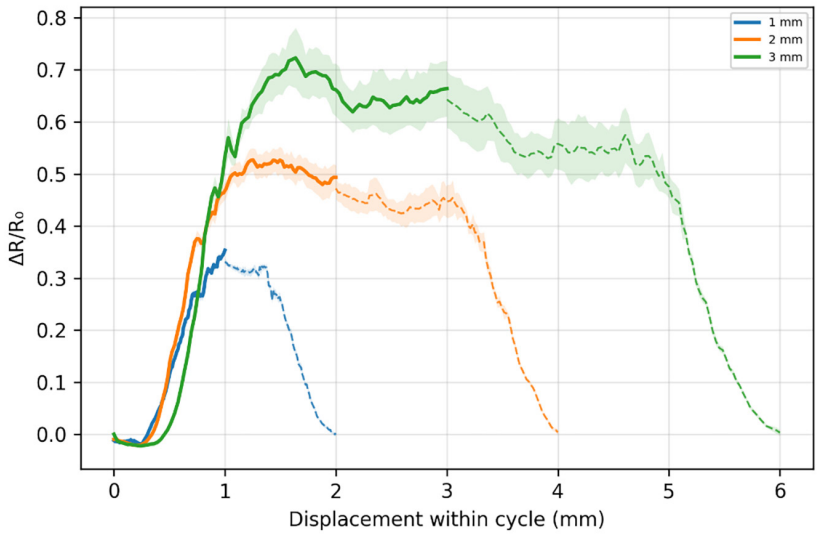

Fig. 5. Relative resistance changes $\Delta R/R_0$ of the P1 sensor under different displacement conditions

The solid line represents the stretching phase, and the dashed line represents the releasing phase, while the shaded areas indicate the standard deviation ranges.

Figure 6 presents how the relative resistance change ($\Delta R/R_0$) varies with displacement for the P2 composite sensor at displacement amplitudes of 3, 4, 6, 8, and 10 mm. The solid lines represent the stretch phase, the dashed lines represent the release phase, and the shaded areas denote the standard deviation ranges. Across all conditions, the $\Delta R/R_0$ increased proportionally with displacement. The peak value rose gradually from approximately 0.17 at 3 mm to 0.24 at 8 mm, but slightly decreased at 10 mm, suggesting that the conductive network may approach saturation or reorganization limits at larger deformations.

In addition, evident hysteresis behavior was observed in all displacement cycles. For a given displacement, the release curves showed lower $\Delta R/R_0$ values compared with the stretch curves, and the hysteresis gap increased with displacement amplitude. Overall, the P2 sensor maintained low variability, with a maximum standard deviation of approximately ± 0.018 under the 10 mm condition, demonstrating superior stability and strain recoverability compared to the P1 sensor.

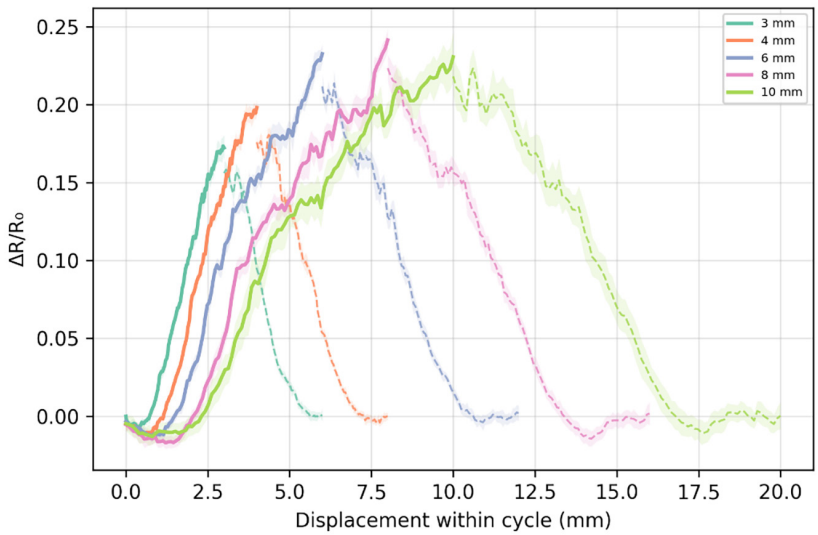

Fig. 6. Relative resistance change $\Delta R/R_0$ of the P2 sensor under different displacement conditions

The solid line represents the stretching phase, and the dashed line represents the releasing phase, while the shaded areas indicate the standard deviation ranges.

Figure 7 shows the comparison of the output curves of the P1 and P2 sensors under the same 3 mm displacement condition. The results indicate that the maximum relative resistance change ($\Delta R/R_0$) of P1 is approximately 0.70, whereas that of P2 is only about 0.17, demonstrating that P1 exhibits higher sensitivity under the same deformation. This difference may reflect more pronounced extension and microcrack formation in the conductive network of P1 during stretching. Both sensors exhibit hysteresis, with the unloading curves lying below the stretching curves; however, the hysteresis magnitude of P2 is smaller, suggesting that its conductive structure exhibits more stable recovery behavior during unloading. Overall, both sensors maintain low standard deviation ranges, indicating a certain degree of repeatability during cyclic measurements.

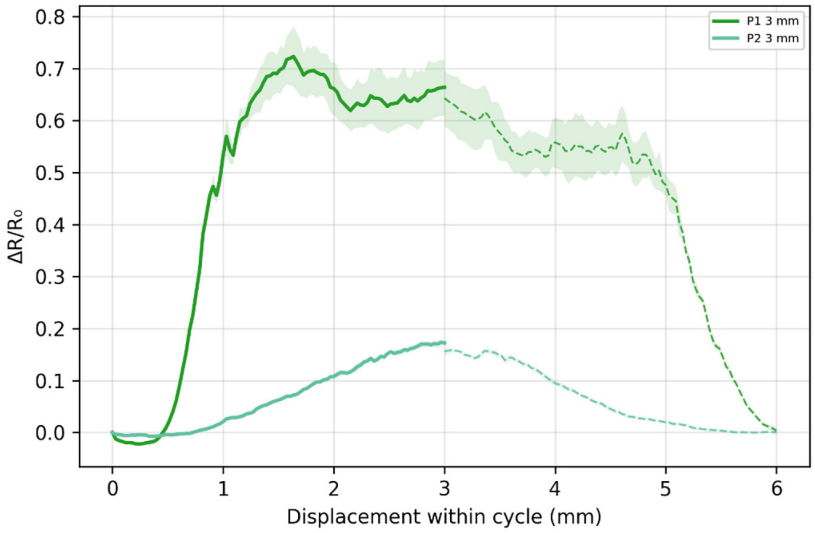

Fig. 7. Comparative performance of P1 and P2 sensors under a 3 mm displacement condition

4.2 Feasibility verification of human attachment

This study further verified the feasibility of attaching the P2 sensor to the human body under realistic wearable conditions. As shown in Figure 8a, the P2 sensor was attached to the dorsal side of the participant's forearm, approximately 12 cm proximal to the wrist dorsal crease, with its longitudinal axis aligned with the forearm direction. A Hi221 wireless 9-axis IMU (Sea-Land Technology) was simultaneously attached to the dorsal surface of the third metacarpal to measure wrist rotation angles. The IMU captured three-axis orientation, angular velocity, and acceleration data, which were transmitted wirelessly to a computer for angle calculation. To ensure stable fixation and prevent cable interference, a 3M Nexcare elastic adhesive band (3M Company) was applied around the dorsal hand.

During testing, the participant rested the forearm on a chair's armrest, keeping the wrist suspended and free from contact. The neutral position (0°) was defined when the palm and forearm were aligned. Downward rotation was defined as a positive angle and upward rotation as a negative angle. Figure 8a illustrates three postures of the hand at –10°, 0°, and 30°. Because upward wrist motion was voluntarily controlled, a slight overshoot occasionally occurred, reaching between –10° and –15°. The participant was instructed to complete approximately five cycles

between 0° and 30° at a slow and consistent speed while avoiding fist clenching or forearm displacement to minimize interference.

As shown in Figure 8b, the resistance variation of the P2 sensor exhibited a high degree of consistency with the IMU angle measurements, demonstrating a synchronous and monotonic trend. When the palm rotated downward, tension was generated on the dorsal forearm skin, leading to an increase in resistance; conversely, when returning to the neutral position, the resistance decreased as the tension was released. The peak and valley positions across repeated cycles showed good repeatability without noticeable baseline drift, indicating that the P2 sensor can stably and reliably track wrist joint movements under skin-attached conditions.

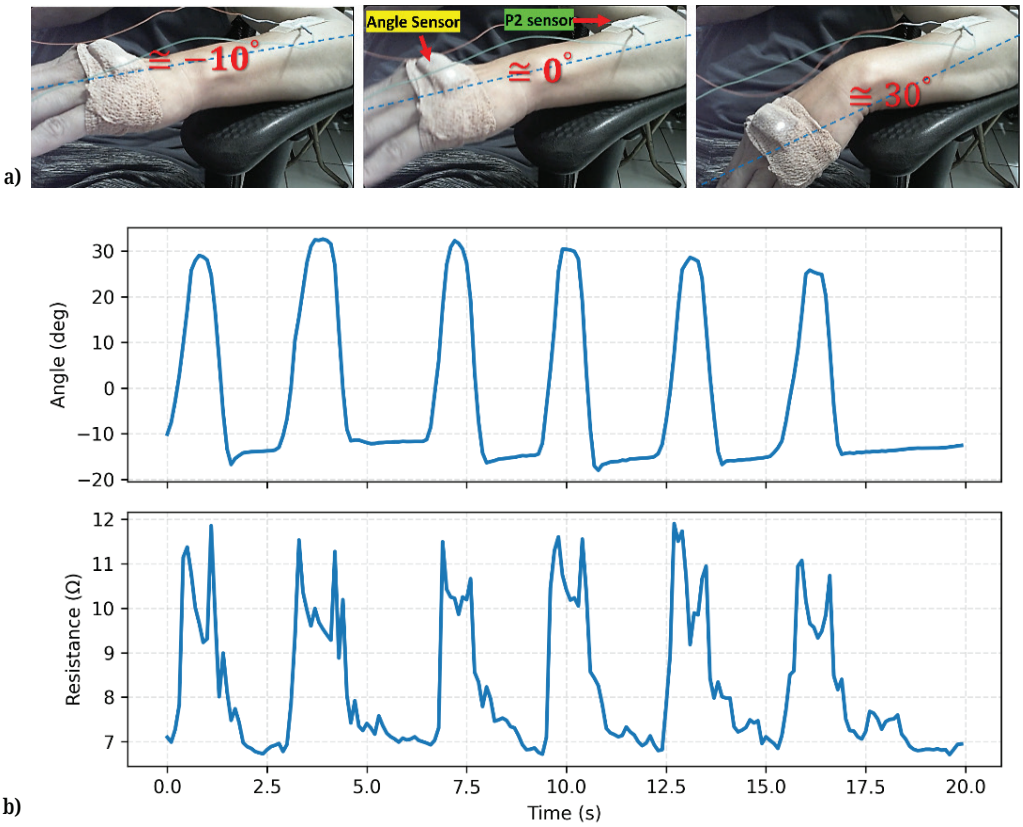

Fig. 8. Wrist motion test with the P2 wearable strain sensor: (a) wrist postures and sensor placement, and (b) corresponding IMU angle signal and sensor resistance variation during repetitive wrist motion

5 DISCUSSIONS

Both sensors developed in this study employed silicone-based conductive composites as their core material. The internal conductive pathways were rearranged during stretching deformation, causing variations in resistance ($\Delta R/R_0$) that reflected the degree of external strain. The two sensor types differed in structural design: P1 focused on higher output sensitivity within a small displacement range, whereas P2 incorporated a layered configuration combining double-sided silicone adhesion and an artificial skin substrate. This structure provided additional mechanical support and guided conductive layer recovery, thereby achieving an extended measurement range and improved output stability.

Experimental results showed that P1 exhibited a pronounced response within the 1–3 mm displacement range, reaching a $\Delta R/R_0$ of approximately 0.70 at 3 mm. However, beyond this range, the response became unstable, and the measurable range was limited. In contrast, P2 maintained stable performance over a wider range extending from 3 to 10 mm, with $\Delta R/R_0$ values between 0.17–0.24. The maximum standard deviation during repeated cycles was approximately 0.018, indicating good repeatability and stability even under larger displacements.

In terms of hysteresis behavior, Figure 9 shows distinct trends between the two sensor types. The hysteresis index of P1 increases rapidly from approximately 0.07 to 0.26 within the 1–3 mm displacement range, whereas P2 exhibits a relatively gradual increase from 0.03 to 0.26 across the 3–10 mm range. The most notable contrast appears under the 3 mm condition, where P1 shows a hysteresis value of about 0.26, significantly higher than P2's 0.03. This indicates that the multilayer composite structure of P2 effectively suppresses hysteresis under low-to-moderate strain conditions. However, as the displacement increased to 10 mm, the hysteresis amplitude of P2 approached the level observed for P1 at 3 mm.

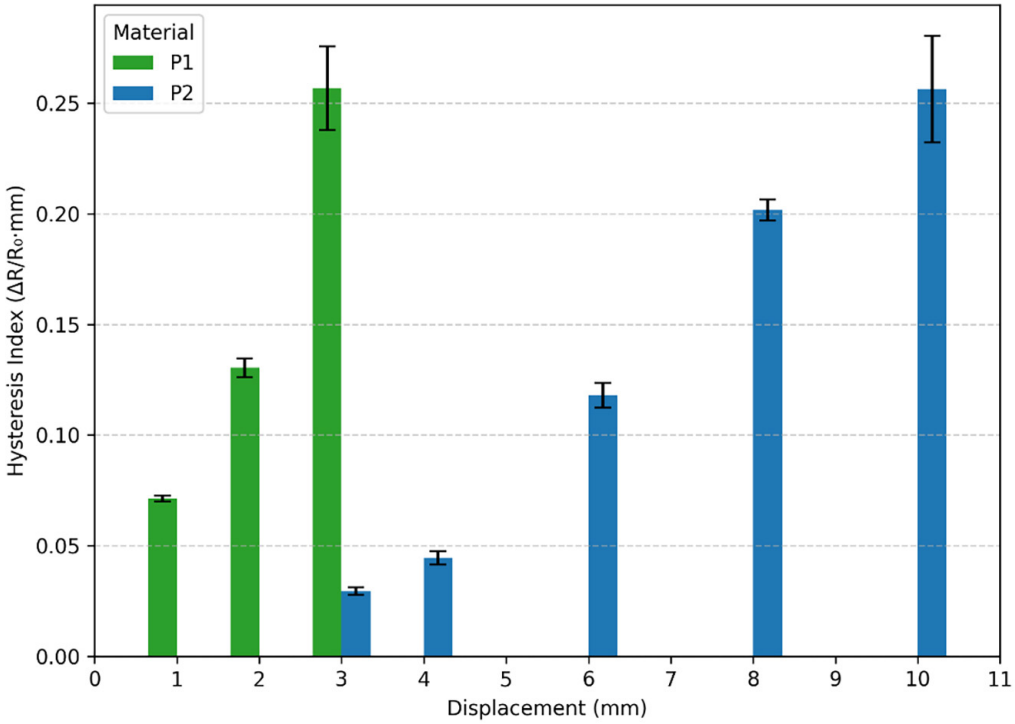

Fig. 9. Comparison of the hysteresis index of sensors P1 and P2 under different displacement conditions (Data are presented as mean ± standard deviation)

In the wrist-mounted motion tracking tests, although the resistance response of P2 exhibited larger fluctuations influenced by biomechanical factors such as skin tension, shear deformation, and localized wrinkling, the signal remained well synchronized with and showed a consistent trend relative to the IMU-derived angular reference. This result indicates that P2 is capable of stable operation under complex and dynamic skin-contact conditions, demonstrating its feasibility as a wearable sensing component for motion monitoring. Overall, the multilayer configuration of P2 effectively balances adhesion performance, output stability, sensing range, and hysteresis suppression, making it more suitable for motion tracking applications

involving high joint mobility. Future work may further investigate skin–material interaction behavior, long-term wear comfort, and anatomical variation across different body sites, while incorporating signal processing or calibration strategies to enhance practical performance in applications such as health monitoring, rehabilitation feedback, and athletic performance assessment.

6 CONCLUSION

This study proposes a relatively simple and cost-effective fabrication approach that integrates 3D silicone printing technology with a multilayer composite structural design, aiming to provide a feasible solution for reducing hysteresis effects and expanding the measurement range of flexible strain sensors. Two types of sensors were developed: a single-layer conductive silicone sensor (P1) and a composite conductive silicone sensor (P2). Through systematic performance comparisons, the results indicate that P2 exhibits a lower hysteresis index and better cyclic stability than P1 within moderate displacement ranges, demonstrating the potential advantages of the proposed multilayer composite structure. Specifically, at 3 mm displacement, the hysteresis index was significantly reduced from 0.26 (P1) to 0.03 (P2), representing an 88% improvement. Additionally, P2 extended the measurable displacement range to 10 mm while maintaining a maximum standard deviation of approximately ±0.018. In the human attachment tests, the P2 sensor successfully tracked wrist joint movements with good synchronization, confirming its feasibility for wearable strain-sensing applications. Although the present work remains at an early stage, the design concept and fabrication strategy demonstrated in this study may serve as a valuable reference for the future development of flexible strain sensors.

7 REFERENCES

[1] M. Amjadi, K. U. Kyung, I. Park, and M. Sitti, "Stretchable, skin-mountable, and wearable strain sensors and their potential applications: A review," *Advanced Functional Materials*, vol. 26, no. 11, pp. 1678–1698, 2016. https://doi.org/10.1002/adfm.201504755

[2] T. Q. Trung and N. E. Lee, "Flexible and stretchable physical sensor integrated platforms for wearable human-activity monitoring and personal healthcare," *Advanced Materials*, vol. 28, no. 22, pp. 4338–4372, 2016. https://doi.org/10.1002/adma.201504244

[3] X. W. Wang, Z. Liu, and T. Zhang, "Flexible sensing electronics for wearable/attachable health monitoring," *Small*, vol. 13, no. 25, 2017. https://doi.org/10.1002/smll.201602790

[4] J. C. Yang, J. Mun, S. Y. Kwon, S. Park, Z. Bao, and S. Park, "Electronic skin: Recent progress and future prospects for skin-attachable devices for health monitoring, robotics, and prosthetics," *Advanced Materials*, vol. 31, no. 48, p. 1904765, 2019. https://doi.org/10.1002/adma.201904765

[5] N. I. Sonil, Z. Ullah, J. Chen, and G. P. Wang, "Wearable strain sensors for human motion detection and health monitoring based on hybrid graphite-textile flexible electrodes," *Journal of Materials Research and Technology*, vol. 26, pp. 764–774, 2023. https://doi.org/10.1016/j.jmrt.2023.07.185

[6] M. S. Tasjid and A. A. Marouf, "Leveraging smartphone sensors for detecting abnormal gait for smart wearable mobile technologies," *International Journal of Interactive Mobile Technologies (iJIM)*, vol. 15, no. 24, pp. 167–175, 2021. https://doi.org/10.3991/ijim.v15i24.25891

[7] B. G. Mohammed and D. S. Hasan, "Smart healthcare monitoring system using IoT," *International Journal of Interactive Mobile Technologies (iJIM)*, vol. 17, no. 1, pp. 141–152, 2023. https://doi.org/10.3991/ijim.v17i01.34675

[8] H. Souri *et al.*, "Wearable and stretchable strain sensors: Materials, sensing mechanisms, and applications," *Advanced Intelligent Systems*, vol. 2, no. 8, p. 2000039, 2020. https://doi.org/10.1002/aisy.202000039

[9] Y. Liu, H. Wang, W. Zhao, M. Zhang, H. Qin, and Y. Xie, "Flexible, stretchable sensors for wearable health monitoring: Sensing mechanisms, materials, fabrication strategies and features," *Sensors*, vol. 18, no. 2, p. 645, 2018. https://doi.org/10.3390/s18020645

[10] X. Huang *et al.*, "High-stretchability and low-hysteresis strain sensors using origami-inspired 3D mesostructures," *Science Advances*, vol. 9, no. 34, p. eadh9799, 2023. https://doi.org/10.1126/sciadv.adh9799

[11] F. Xue *et al.*, "Ultra-sensitive, highly linear, and hysteresis-free strain sensors enabled by gradient stiffness sliding strategy," *Npj Flexible Electronics*, vol. 8, no. 1, p. 14, 2024. https://doi.org/10.1038/s41528-024-00301-7

[12] C. Yan *et al.*, "Highly stretchable piezoresistive graphene–nanocellulose nanopaper for strain sensors," *Advanced Materials*, vol. 26, no. 13, pp. 2022–2027, 2014. https://doi.org/10.1002/adma.201304742

[13] M. Amjadi, A. Pichitpajongkit, S. Lee, S. Ryu, and I. Park, "Highly stretchable and sensitive strain sensor based on silver nanowire–elastomer nanocomposite," *ACS Nano*, vol. 8, no. 5, pp. 5154–5163, 2014. https://doi.org/10.1021/nn501204t

[14] R. Guo *et al.*, "Biomimicking topographic elastomeric petals (e-petals) for omnidirectional stretchable and printable electronics," *Advanced Science*, vol. 2, no. 3, p. 1400021, 2015. https://doi.org/10.1002/advs.201400021

[15] E. Roh, B.-U. Hwang, D. Kim, B.-Y. Kim, and N.-E. Lee, "Stretchable, transparent, ultrasensitive, and patchable strain sensor for human–machine interfaces comprising a nanohybrid of carbon nanotubes and conductive elastomers," *ACS Nano*, vol. 9, no. 6, pp. 6252–6261, 2015. https://doi.org/10.1021/acsnano.5b01613

[16] S. Zhao *et al.*, "Recent advancements in flexible and stretchable electrodes for electromechanical sensors: Strategies, materials, and features," *ACS Applied Materials & Interfaces*, vol. 9, no. 14, pp. 12147–12164, 2017. https://doi.org/10.1021/acsami.6b13800

[17] G. Shi *et al.*, "Highly sensitive, wearable, durable strain sensors and stretchable conductors using graphene/silicon rubber composites," *Advanced Functional Materials*, vol. 26, no. 42, pp. 7614–7625, 2016. https://doi.org/10.1002/adfm.201602619

[18] B. Liang *et al.*, "Ultra-stretchable and highly sensitive strain sensor based on gradient structure carbon nanotubes," *Nanoscale*, vol. 10, no. 28, pp. 13599–13606, 2018. https://doi.org/10.1039/C8NR02528B

[19] Y. Zheng *et al.*, "The effect of filler dimensionality on the electromechanical performance of polydimethylsiloxane based conductive nanocomposites for flexible strain sensors," *Composites Science and Technology*, vol. 139, pp. 64–73, 2017. https://doi.org/10.1016/j.compscitech.2016.12.014

[20] J. F. Christ, N. Aliheidari, A. Ameli, and P. Pötschke, "3D printed highly elastic strain sensors of multiwalled carbon nanotube/thermoplastic polyurethane nanocomposites," *Materials & Design*, vol. 131, pp. 394–401, 2017. https://doi.org/10.1016/j.matdes.2017.06.011

[21] Y. Wang *et al.*, "Flexible electrically resistive-type strain sensors based on reduced graphene oxide-decorated electrospun polymer fibrous mats for human motion monitoring," *Carbon*, vol. 126, pp. 360–371, 2018. https://doi.org/10.1016/j.carbon.2017.10.034

[22] D. Niu *et al.*, "Graphene-elastomer nanocomposites based flexible piezoresistive sensors for strain and pressure detection," *Materials Research Bulletin*, vol. 102, pp. 92–99, 2018. https://doi.org/10.1016/j.materresbull.2018.02.005

[23] Z. Zhang *et al.*, "Electromechanical performance of strain sensors based on viscoelastic conductive composite polymer fibers," *ACS Applied Materials & Interfaces*, vol. 14, no. 39, pp. 44832–44840, 2022. https://doi.org/10.1021/acsami.2c12120

[24] X. Wu, Y. Han, X. Zhang, Z. Zhou, and C. Lu, "Large-area compliant, low-cost, and versatile pressure-sensing platform based on microcrack-designed carbon black@polyurethane sponge for human–machine interfacing," *Advanced Functional Materials*, vol. 26, no. 34, pp. 6246–6256, 2016. https://doi.org/10.1002/adfm.201601995

[25] Z. Wang *et al.*, "Polyurethane/Cotton/carbon nanotubes core-spun yarn as high reliability stretchable strain sensor for human motion detection," *ACS Applied Materials & Interfaces*, vol. 8, no. 37, pp. 24837–24843, 2016. https://doi.org/10.1021/acsami.6b08207

[26] H. Jeon, S. K. Hong, M. S. Kim, S. J. Cho, and G. Lim, "Omni-purpose stretchable strain sensor based on a highly dense nanocracking structure for whole-body motion monitoring," *ACS Applied Materials & Interfaces*, vol. 9, no. 48, pp. 41712–41721, 2017. https://doi.org/10.1021/acsami.7b14153

[27] L. Duan, D. R. D'Hooge, and L. Cardon, "Recent progress on flexible and stretchable piezoresistive strain sensors: From design to application," *Progress in Materials Science*, vol. 114, p. 100617, 2020. https://doi.org/10.1016/j.pmatsci.2019.100617

[28] T. Nishikawa, H. Yamane, N. Matsuhisa, and N. Miki, "Stretchable strain sensor with small but sufficient adhesion to skin," *Sensors*, vol. 23, no. 4, p. 1774, 2023. https://doi.org/10.3390/s23041774

[29] L. Zheng, D. Liu, J. Dai, Z. Hao, W. Wu, and X. Yin, "Flexible antibacterial strain sensor with low electrical hysteresis, ultralow detection limit, and wide linear sensing range for human motion monitoring and human–machine interaction," *Chemical Engineering Journal*, vol. 500, p. 157289, 2024. https://doi.org/10.1016/j.cej.2024.157289

[30] H. Park *et al.*, "Stretchable array of highly sensitive pressure sensors consisting of polyaniline nanofibers and au-coated polydimethylsiloxane micropillars," *ACS Nano*, vol. 9, no. 10, pp. 9974–9985, 2015. https://doi.org/10.1021/acsnano.5b03510

[31] Y. Cheng, R. Wang, J. Sun, and L. Gao, "A stretchable and highly sensitive graphene-based fiber for sensing tensile strain, bending, and torsion," *Advanced Materials*, vol. 27, no. 45, pp. 7365–7371, 2015. https://doi.org/10.1002/adma.201503558

[32] K.-H. Kim, D.-W. Jeong, N.-S. Jang, S.-H. Ha, and J.-M. Kim, "Extremely stretchable conductors based on hierarchically-structured metal nanowire network," *RSC Advances*, vol. 6, no. 62, pp. 56896–56902, 2016. https://doi.org/10.1039/C6RA09644A

[33] S. Zhao *et al.*, "Binary synergistic sensitivity strengthening of bioinspired hierarchical architectures based on fragmentized reduced graphene oxide sponge and silver nanoparticles for strain sensors and beyond," *Small*, vol. 13, no. 28, p. 1700944, 2017. https://doi.org/10.1002/smll.201700944

[34] X. Wu, Y. Han, X. Zhang, and C. Lu, "Spirally structured conductive composites for highly stretchable, robust conductors and sensors," *ACS Applied Materials & Interfaces*, vol. 9, no. 27, pp. 23007–23016, 2017. https://doi.org/10.1021/acsami.7b06256

[35] J. Zhu, J. J. Fox, N. Yi, and H. Cheng, "Structural design for stretchable microstrip antennas," *ACS Applied Materials & Interfaces*, vol. 11, no. 9, pp. 8867–8877, 2019. https://doi.org/10.1021/acsami.8b22021

[36] P. Zhu *et al.*, "Skin-electrode iontronic interface for mechanosensing," *Nature Communications*, vol. 12, no. 1, p. 4731, 2021. https://doi.org/10.1038/s41467-021-24946-4

[37] D. Zhong *et al.*, "High-speed and large-scale intrinsically stretchable integrated circuits," *Nature*, vol. 627, no. 8003, pp. 313–320, 2024. https://doi.org/10.1038/s41586-024-07096-7

[38] Y. Gao, L. Yu, J. C. Yeo, and C. T. Lim, "Flexible hybrid sensors for health monitoring: Materials and mechanisms to render wearability," *Advanced Materials*, vol. 32, no. 15, p. 1902133, 2020. https://doi.org/10.1002/adma.201902133

8 AUTHOR

Jiun-Hung Lin received his M.S. in Electronic Engineering from I-Shou University (2000) and his Ph.D. in Medical Electronics from the Institute of Biomedical Engineering at National Yang Ming University (2006). Since 2023, he has served as an Assistant Professor in the Department of Electronic Engineering (First Campus) at National Kaohsiung University of Science and Technology. In 2024, he also assumed the role of director of the Maker Center under the Office of Innovation and Entrepreneurship. His research interests include automated system design, assistive technology development, applications of intelligent algorithms, and sound signal processing (E-mail: jhlin001@nkust.edu.tw).